Journal of Energy Storage 112 (2025) 115474

Contents lists available at ScienceDirect

Journal of Energy Storage

journal homepage: www.elsevier.com/locate/est

Research papers

Taking bio-induced precipitation to the field for sustainable geo-energy storage: Experimental and numerical studies of leakage mitigation

Olufemi Olorode [a,*], Oladoyin Kolawole [b], Chibuzor Igweonu [a], Harun Rashid [c]

[a] Craft & Hawkins Department of Petroleum Engineering, Baton Rouge, LA 70803, USA
[b] John A. Reif, Jr. Department of Civil and Environmental Engineering, New Jersey Institute of Technology, Newark, NJ 07102, USA
[c] Los Alamos National Laboratory, Los Alamos, NM 87545, USA

ARTICLE INFO

Keywords:
CCUS
Hydrogen storage
Bioenergy
Underground gas storage
Underground gas leakage mitigation

ABSTRACT

There is a consensus that geologic hydrogen and CO_2 storage as critical geo-energy technologies will play a significant role in meeting the 2050 net-zero global carbon emission target. However, the potential leakage of stored CO_2 and hydrogen from the subsurface to shallower rocks or atmosphere through the faults/fractures expected in most subsurface rocks poses significant environmental and safety concerns. We propose reducing the permeability along these faults/fractures to curtail the gas leakage. This work presents the first-of-a-kind development of experimentally validated core-to-field-scale numerical models for studying the application of a biologically induced mineral precipitation (BIMP) technology to mitigate the leakage of the stored CO_2 and hydrogen from these subsurface rocks. Further, we proposed a novel approach for estimating the field-scale CO_2 and hydrogen gas storage efficiencies of applied BIMP technology for sealing the fractures/faults that serve as the leakage pathways. Relative to the core-scale experiments, our numerical model showed an accuracy of 95 % in the permeability reduction. We quantified CO_2 and hydrogen leakage through natural fractures at the field scale and observed a natural fracture permeability reduction of up to 100 % after the BIMP treatment for the fractures closest to the horizontal treatment well. Finally, the results after the BIMP treatment indicate an increase in the long-term CO_2 storage efficiency from 50 % to 77 % over 1100 years relative to pre-treatment, while the BIMP treatment increases the efficiency from 65 % to 87 % for 25-year cyclic storage and production of hydrogen. In conclusion, this work presents the first experimentally validated core-to-field-scale model for the application of BIMP to improve storage efficiency.

1. Introduction

Geologic carbon dioxide storage or sequestration (GCS) is the process of storing carbon dioxide (CO_2) in subsurface formations such as depleted hydrocarbon reservoirs, aquifers, and salt caverns [1–5]. GCS is needed to support decarbonization efforts, enhance energy security, mitigate climate change, and facilitate the transition towards low-carbon and green energy sources. Additionally, GCS plays a significant role in carbon capture and storage [5–17]. In this context, CO_2, which accounts for ~80 % of all greenhouse gases, is captured from industrial processes or directly from the air and stored in various subsurface geologic formations [1–3,5,17,18]. GCS can significantly contribute to mitigating anthropogenic climate change by reducing the amount of CO_2 released into the atmosphere [19–21]. Deep saline aquifers are permeable salt-water-bearing rocks with enormous potential for storing CO_2 and other gases like hydrogen. However, they require careful monitoring to prevent gas leakage into shallower groundwater sources [22,23]. The importance of geologic gas (CO_2 or hydrogen) storage extends beyond climate change mitigation. It also contributes to the transition to a more sustainable and green energy future by enabling the storage of renewable energy sources. Geologic hydrogen storage (GHS) involves storing hydrogen in underground formations, such as deep saline aquifers, depleted hydrocarbon reservoirs, or salt caverns [24,25]. Its advantages over surface storage include its smaller surface footprint, safety, minimal environmental impacts, longer operating lifetimes, higher pressures and storage volumes, and reduced investment costs [26–28]. Geologic CO_2 and hydrogen leakage pose significant environmental, safety, and efficiency concerns. CO_2 leakage undermines the purpose of geologic storage because of the potential release of the stored gases back into the atmosphere.

---

* Corresponding author.
E-mail address: folorode@lsu.edu (O. Olorode).

https://doi.org/10.1016/j.est.2025.115474
Received 24 June 2024; Received in revised form 5 November 2024; Accepted 17 January 2025

Various researchers have reported the potential of using biologically induced mineral precipitation (BIMP) to treat near-wellbore leakage, reduce gas–related corrosion in underground infrastructure, and lower the risk of unwanted migration of gases and other fluids in the subsurface [5,29–31]. However, most of these studies have focused on core-scale experiments, while a few have simulated idealistic reservoirs that contained no pre-existing fractures and ignored the magnitude of pressures induced during the BIMP process. The most popular BIMP technologies are microbially-induced carbonate precipitation (MICP) [5,15,29–31] and enzyme-induced carbonate precipitation (EICP) [32,33], and this current study focuses on using MICP as the biomineralization technology. BIMP has been reported to seal fractures in oil-well cement and to modify near-wellbore reservoir rock permeability [5,29,30,34]. In Phillips et al. [29], BIMP was adopted as a mitigation technology to seal high permeability regions around injection wells in a sandstone formation, and the result showed a significant permeability decrease with a range of 2 to 4 orders of magnitude in the sandstone studied. BIMP was further investigated in a sandstone formation to characterize a failed waterflood injection well and evaluate its potential to reduce permeability at the field scale [30]. The results show that after six days (144 h) of alternating injections of the microbes and cementation materials, the injectivity decreased by approximately 70 % [30].

To assess the long-term CO_2 storage security and potential leakage in geologic formations, an experimental study [5,35] examined rock-CO_2-microbial interaction and its implication for CO_2 storage in carbonate-rich rocks. The work also evaluated the potential of BIMP as a post-injection remediation strategy to mitigate CO_2 leakage and achieve long-term containment in carbonate formations. Findings in the work [35] suggested that without a post-injection treatment like BIMP, CO_2 could leak through carbonate reservoirs and potentially create future environmental concerns. Landa-Marbán et al. [36] numerically simulated the critical processes involved in BIMP, and their results indicated that the BIMP technology can plug a leakage pathway at a considerable distance from the injection well. However, their purely numerical study focused only on CO_2 leakage through a single vertical fracture and it did not address the high pressures induced because of the high injection rates and reduced permeability near the injection well. Unfortunately, these high pressures will curtail the application of these simulation results in the field because of the high risk of fracturing subsurface formations when the pore pressure exceeds the minimum principal stress in the rock. So, there is a significant knowledge gap on how to apply field-scale BIMP treatment to curtail leakage through fractures/faults in the caprocks of geologic formations used for permanent CO_2 sequestration or cyclic hydrogen storage and production.

Additionally, the approach presented by Landa-Marbán et al. [36] to quantify the effectiveness of a field-scale BIMP treatment was limited to estimating the CO_2 leakage rate over 30 days through the single fracture in their model. Although the change in this leakage rate before and after BIMP indicates the effectiveness of the BIMP treatment, it is not a proxy for storage efficiency because a reduction in CO_2 leakage rate over 30 days does not indicate the prevention of gas leakage over the long durations expected during GCS and cyclic GHS and production. To the best of the authors' knowledge, there is no published approach to estimate the improvement in storage efficiency associated with BIMP.

This novel work is the first to: (a) propose experimentally validated core-to-field-scale numerical models for evaluating the potential of BIMP in curtailing leakage through fractured caprocks applicable to underground CO_2 and hydrogen storage; (b) develop and propose an approach to estimate the field-scale CO_2 and hydrogen gas storage efficiencies based on BIMP strategy. Most underground rocks are naturally fractured to an extent, and there is currently no technology to determine the location, size, and orientation of all fractures in the subsurface. So, our demonstration of the sealing of forty stochastic natural fractures (with arbitrary fracture properties) in a model fractured caprock illustrates the applicability of the BIMP in real fields. The following sections of this paper will discuss the materials and methods, experimental results, model validation against experimental data, and the field application of BIMP technology to curtail CO_2 and hydrogen leakage.

2. Materials and methods

2.1. Experimental program

The laboratory experiments performed in this study were performed on subsurface limestone core samples. The core samples are permeable (2.46–3.30 mD) and porous (8–9 %) limestone rocks containing natural microfractures. The limestone core samples were cut sub-parallel to the bedding plane before testing and later saturated with brine for 24 h. The brine used is similar in composition to the formation water in the San Andres formation in the Central Basin Platform, USA, where the core samples were extracted.

The BIMP treatment used for the experiment presented in this study followed the established procedure for such treatment reported in Kolawole et al. [5,15,34]. The biological agent (microbe) used in the experimental BIMP treatment in this study is *Sporosarcina pasteurii* (ATCC® 11859™), an aerobic microbe that was grown with Luria Broth at 33 °C inside a Lab-Line 4628 Incubated Orbital Shaker at 220 rpm for 24 h [5,35,37]. We prepared the microbial culture with distilled water to prevent the impact of salinity or impurities on the biomineralization process in rocks. The BIP treatment using *Sporosarcina pasteurii* involves the production of an enzyme called "urease" during its metabolism. This catalyzes the hydrolysis of urea [$CO(NH_2)_2$] to form carbonate (CO_3^{2-}) and ammonium (NH_4^+) ions, which, in the presence of calcium ions (Ca^{2+}), undergo a kinetic reaction to precipitate calcium carbonate ($CaCO_3$, calcite mineral) crystals [5,15,31]. The BIMP process using *Sporosarcina pasteurii* is summarized as follows [5,15,34]:

$$CO(NH_2)_2 + 2H_2O \overset{\text{urease}}{\rightarrow} 2NH_4{}^{+} + CO_3{}^{2-}, \tag{1}$$

$$Ca^{2+} + \text{cell} \rightarrow \text{Cell}\cdot Ca^{2+}, \tag{2}$$

$$\text{Cell}\cdot Ca^{2+} + CO_3{}^{2-} \rightarrow \text{Cell}\cdot CaCO_3\ (s). \tag{3}$$

We conducted the experimental study of the BIMP process using a Hassler-type core holder and a Volume-Pressure-Actuator (VPA) dual syringe pump to push distinct aqueous media into the core samples at high pressure and constant ultra-precise flow rate, as illustrated in the injection treatment schematic in Fig. 1. The cultured microbial solution (m) was first injected continuously for 24 h into the limestone core samples inserted firmly inside a rubber sleeve in the core holder. We injected the microbial solution at a constant injection rate of 5 ml/min with a 7.5 MPa confining pressure, after which the pump pressure was equilibrated to a value of 5.2 MPa. The core holder's outlet and inlet valves were then shut in (S_m) for 1 h to allow the microbes to saturate the pores in the limestone core samples further. Next, we shut in the syringe pump's outlet and connected the inlet valves of the core holder to the oxygen gas cylinder.

Using a high-pressure regulator mounted on top of the gas cylinder, we continuously injected oxygen (O) for 24 h to enable the growth of the aerobic microbe that invaded the pores and microfractures in the limestone core sample. We then shut the core holder's inlet connection valve to discontinue the oxygen injection for 1 h. Next, we reopened the core holder's inlet valve while simultaneously opening the syringe pump's outlet valve to allow the injection of an equimolar cementation solution (u) of urea [$CO(NH_2)_2$] and calcium chloride ($CaCl_2$) into the limestone core sample for 24 h. Finally, all the inlet valves into the core holder were shut in for 646 h (26.9 days) to allow the kinetic biomineralization reaction to precipitate calcium carbonate crystals and complete a 720 (30 days) BIMP treatment.

We measured permeability on the core samples before and after the BIMP treatment using nitrogen gas at 300 psi and with 30 psi pressure steps. We estimated the permeability of the core samples using the

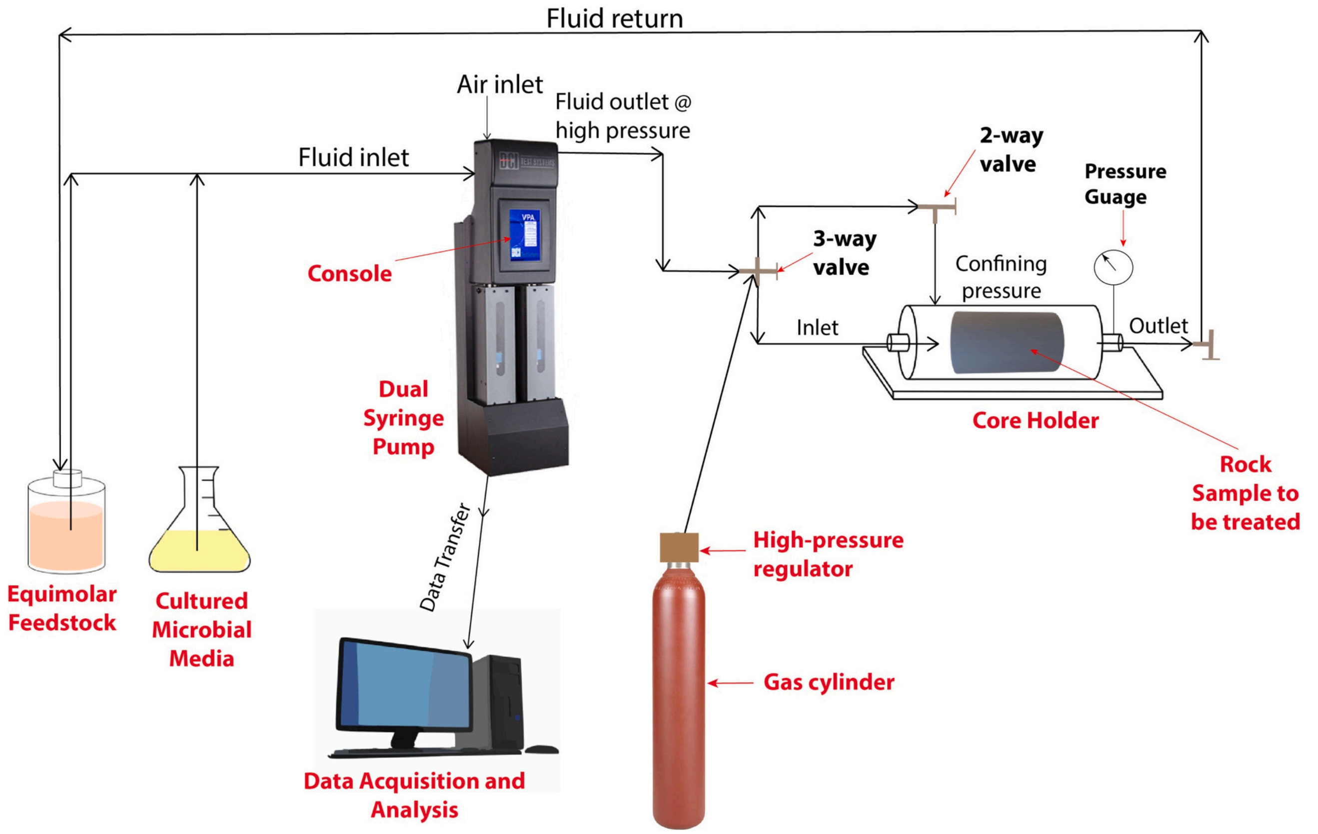

Fig. 1. The schematic of the bio-induced mineralization treatment experiment.

modified Pulse Decay method from Brace et al. (1968) [38], as follows:

$$\alpha = \frac{kA}{\mu\beta L}\left(\frac{1}{V_1}+\frac{1}{V_2}\right), \tag{4}$$

where α is the slope of the decay on the plot of $\ln(\Delta P/\Delta P_0)$ vs. time, k is the permeability, A is the cross-sectional area of the sample, L is the length of the sample, μ is the fluid viscosity, β is the isothermal gas compressibility at given temperature and pressure conditions, V_1 is the downstream reservoir volume, and V_2 is the upstream reservoir volume. If the downstream reservoir volume V_1 is assumed to be constant throughout the test, the permeability can be estimated as follows:

$$k = \frac{\alpha\mu\beta L V_1}{A}, \tag{5}$$

The next section presents the mathematical model developed to simulate the BIMP process at the core and field scales.

2.2. Bio-induced mineral precipitation model development

In this work, the mathematical model for BIMP focuses on oxygen and urea because they are the rate-limiting components in the microbial growth and cementation processes. This approach was adopted because it is more computationally expensive than fully coupled reactive transport models.

2.2.1. Single-phase water flow equation

The equation governing the single-phase flow of water is the mass conservation equation, which is given as follows:

$$\frac{\partial\phi}{\partial t} + \nabla . v_w = q_w, \tag{6}$$

where the water velocity (v_w) is given by Darcy's law as follows:

$$v_w = -\frac{K}{\mu_w}(\nabla P_w - \rho_w g). \tag{7}$$

Here, ϕ is porosity, q_w is the source or sink term, K is the absolute permeability of the rock, μ_w is water viscosity, P_w is pressure, ρ_w is water density, and g is the acceleration due to gravity.

2.2.2. Compositional transport equations

The movement of suspended microbes, oxygen, and urea in the porous medium is modeled using a set of advection-dispersion-reaction equations as follows:

$$\frac{\partial(C_\xi\phi)}{\partial t} + \nabla . J_\xi = C_\xi q_w + R_\xi, \tag{8}$$

where the dispersive flux (J_ξ) of component ξ is given as:

$$J_\xi = -\phi \boldsymbol{D}_\xi \nabla C_\xi + C_\xi v_w. \tag{9}$$

Here, component ξ represents microbes (m), oxygen (o), and urea (u), respectively. The symbol C_ξ represents the mass concentration or density of component ξ in water, and R_ξ and $\boldsymbol{D}_\xi$ represent the reaction term and dispersion tensor for each component.

2.2.3. Dispersion model

The dispersion of the components ($\boldsymbol{D}_\xi$) in the reservoir is modeled as follows [39]:

$$\boldsymbol{D}_\xi = \propto_T \|v\| I + (\propto_L - \propto_T)\frac{v \otimes v}{\|v\|} + D_\xi I, \tag{10}$$

where D_ξ represents the effective diffusion coefficient for each component, $v = \frac{v_w}{\phi}$ is the interstitial velocity of the aqueous phase, and $\propto_T$ and $\propto_L$ are the transverse and longitudinal dispersion coefficients.

2.2.4. *Solid-phase equations*

The biofilm and calcite are considered immobile and part of the solid phase. So, their governing mass balance equations do not have a (convective or dispersive) flux term. They are given as follows:

$$\frac{\partial\left(\rho_\chi \phi_\chi\right)}{\partial t} = R_\chi, \tag{11}$$

where χ represents the biofilm (b) and calcite (c) components, and ϕ_χ is the porosity associated with each component (χ). The symbols ρ_χ and R_χ represent the density and reaction term for each component (χ).

2.2.5. *Evolution rate of suspended microbes*

The rate of growth and loss of suspended microbes controls their evolution over time. Oxygen consumption and biofilm detachment (because of fluid flow) control microbial growth. In contrast, the microbes' death (because of aging and the attachment of suspended microbes to the pore wall and biofilm) controls the loss of the suspended microbes. Combining these factors, the overall rate of change of the suspended microbes (R_m) is given as follows:

$$R_m = c_m \phi \left(Y\mu \frac{c_o}{k_o + c_o} - k_d - k_a \right) + \phi_b \rho_b k_{str} \phi \left\| \nabla P_w - \rho_w g \right\|^{0.58}, \tag{12}$$

where μ is the maximum specific growth rate, k_o is the half-velocity coefficient for oxygen, Y is the growth yield coefficient, k_{str} is the detachment rate, k_d is the microbial death coefficient, and k_a is the microbial attachment coefficient. The symbol ρ_b represents the biofilm density, c_o and c_m represent the oxygen and microbial concentrations, and ϕ_b is the porosity associated with the biofilm. Mathematically, ϕ_b is equal to the ratio of the pore volume occupied by the biofilm to the bulk volume of the rock.

2.2.6. *Oxygen consumption*

The oxygen consumption rate (R_o) can be expressed as [40]:

$$R_o = -\left(c_m \phi + \rho_b \phi_b\right) F\mu \frac{c_o}{k_o + c_o}, \tag{13}$$

where F is the ratio of the mass of oxygen consumed to the mass of the substrate used for microbial growth.

2.2.7. *Urea conversion*

The urea conversion rate (R_u) is estimated using the Monod equation [41,42]:

$$R_u = -\rho_b\, \phi_b\, \mu_u \frac{c_u}{k_u + c_u}, \tag{14}$$

where c_u is the urea concentration, k_u is the half-velocity coefficient for urea, and μ_u is the maximum urea utilization rate.

2.2.8. *Mineral precipitation*

In calcium-rich formations, the calcite precipitation rate (R_c) tends to be constrained by the relatively slower rate of ureolysis [43]. So, an efficient and accurate approach to estimating the calcite precipitation rate is to approximate it as the negative of the urea utilization rate [44]. This yields:

$$R_c = \rho_b \phi_b Y_{uc} \mu_u \frac{c_u}{k_u + c_u} \tag{15}$$

2.2.9. *Biofilm evolution*

The rate of biofilm evolution (R_b) is given as [36]:

$$R_b = \rho_b \phi_b \left[Y\mu \frac{c_o}{k_o + c_o} - k_d - \frac{R_c}{\rho_c\left(\phi_o - \phi_c\right)} - k_{str} \phi \left\| \nabla P_w - \rho_w g \right\|^{0.58} \right] + c_m \phi k_a, \tag{16}$$

where ϕ_c represents the porosity associated with the calcite. It is the ratio of the pore volume occupied by the calcite to the bulk volume of the rock.

2.2.10. *Dynamic porosity*

The pore spaces in the rock decrease over time because of the deposition of the biofilm and calcite, which are considered immobile and part of the solid phase. The increase in the amount of biofilm and calcite deposited over time results in a corresponding decrease in the dynamic or current porosity value (ϕ) as follows:

$$\phi = \phi_o - \phi_b - \phi_c, \tag{17}$$

where ϕ_o is the initial porosity of the porous medium.

2.2.11. *Porosity-dependent permeability*

The dynamic permeability in this work is estimated from the dynamic porosity (ϕ) using the model presented in [45], which is given as:

$$K = \begin{cases} \left[K_o \left(\dfrac{\phi - \phi_{crit}}{\phi_o - \phi_{crit}} \right)^{\eta} + K_{min} \right] \dfrac{K_o}{K_o + K_{min}}, \phi > \phi_{crit} \\ K_{min},\ \phi \le \phi_{crit} \end{cases}, \tag{18}$$

where K_o represents the initial rock permeability, ϕ_{crit} is the critical porosity at which the permeability reaches its minimum value K_{min}, and η is a factor for adjusting the permeability-porosity relationship.

The governing single-phase flow, compositional transport, and solid-phase equations are discretized using the finite-volume method and solved for the changes in the primary variables (gas-phase pressure, water saturation, and molar concentrations of the microbes, oxygen, urea, biofilm, and calcite) in each timestep using Newton's method. This work leverages the modules in the MATLAB Reservoir Simulation Toolkit (MRST) [46,47] to facilitate the numerical studies performed, and the developed model is generally applicable to field-scale BIMP and incorporates all biologically-induced mineral precipitations and bio-cemented processes at in-situ reservoir conditions. Although this work mostly focuses on the simulation of the BIMP treatment, the last section evaluates the efficiency of the treatment by injecting either CO_2 or hydrogen before and after the treatment. So, it is worth clarifying that we leveraged the two-phase gas-water model in the CO_2 module in MRST to simulate the gas injection period. The primary variables in this model are the gas-phase pressure and water saturation.

3. Experimental results

After conducting the BIMP treatment discussed in Section 2.1, we observed a 67.2 % reduction in permeability from 12.5×10^{-3} mD to 4.11×10^{-3} mD in Limestone sample 1, as shown in Fig. 2a. In Limestone sample 2, a 43.97 % decrease in permeability from 14.03×10^{-2} mD to 7.86×10^{-2} mD was recorded, as shown in Fig. 2b. These permeability reductions can be attributed to the precipitation of calcites in the pore spaces and microfractures in the limestone core. The significant decrease in permeability (40 % - 70 %) suggests that the BIMP treatment can effectively reduce the permeability of a fractured porous medium. This result is consistent with previous studies [5,29,30], which reported a significant reduction in permeability in sandstone formations due to calcite mineral precipitation from BIMP treatment. The extended duration of the BIMP treatment for biomineralization might have contributed to the substantial decrease in permeability because it allowed sufficient time to form the biofilm and induce the calcite mineral precipitation. This calcite precipitation subsequently results in the occlusion of the pore spaces and microfractures in the fractured geologic medium.

The observed reduction in permeabilities from the experimental core-scale results provides supporting evidence for the effectiveness of BIMP as a technology to potentially seal off CO_2 or hydrogen leakage

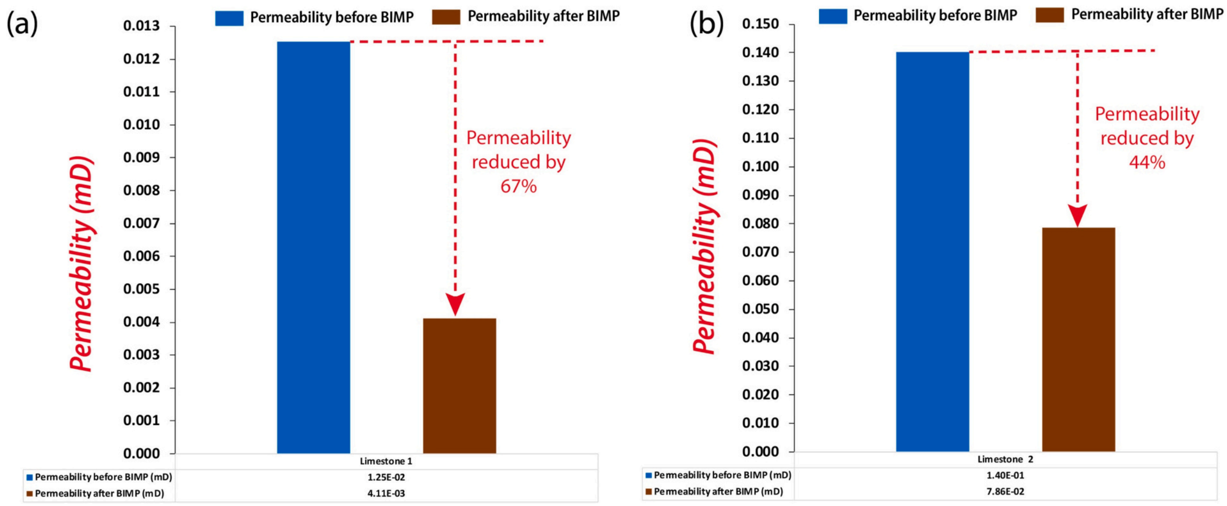

Fig. 2. Permeability of the limestone core before and after the BIMP treatment.

pathways in fractured caprocks. Therefore, BIMP treatment could help curtail CO_2 or hydrogen migration out of storage reservoirs and enhance the security of GCS and GHS. Further discussions on laboratory-scale changes in hydraulic properties (permeability and porosity) of different rocks due to BIMP processes have been reported in the literature [5,15,34,35].

4. Model validation against experimental data

4.1. Core-scale simulation

We simulated a fractured cylindrical domain using unstructured Voronoi grids to validate the numerical BIMP model against the experimental results presented in Section 3. Fig. 3a presents the mesh for the simulation domain, which shows the vertical fracture as a red plane. There are 20 layers and a total of 3003 cells in the simulation domain. In contrast, Fig. 3b shows the permeability in the matrix and fracture cells. The color map is consistent with the significant permeability contrast between the matrix and fracture. The model parameters are based on our experiments and are summarized in Table 1. We defer the discussion of our mesh sensitivity studies to Section 4.2, after describing how we compute the permeabilities used to decide the optimum mesh.

The top of the core was treated as the upstream end and modeled as a constant-pressure (Dirichlet) boundary to mimic the experimental procedure. In contrast, the microbes, oxygen, and urea were injected at a constant rate into the cells at the bottom of the domain. The BIMP process was simulated in six steps, as shown in Fig. 4, but we also simulated a 24-hour injection of water at a fixed rate before and after the BIMP process. The idea is to estimate the average permeability of the sample from the injection rate and pressure difference across the sample

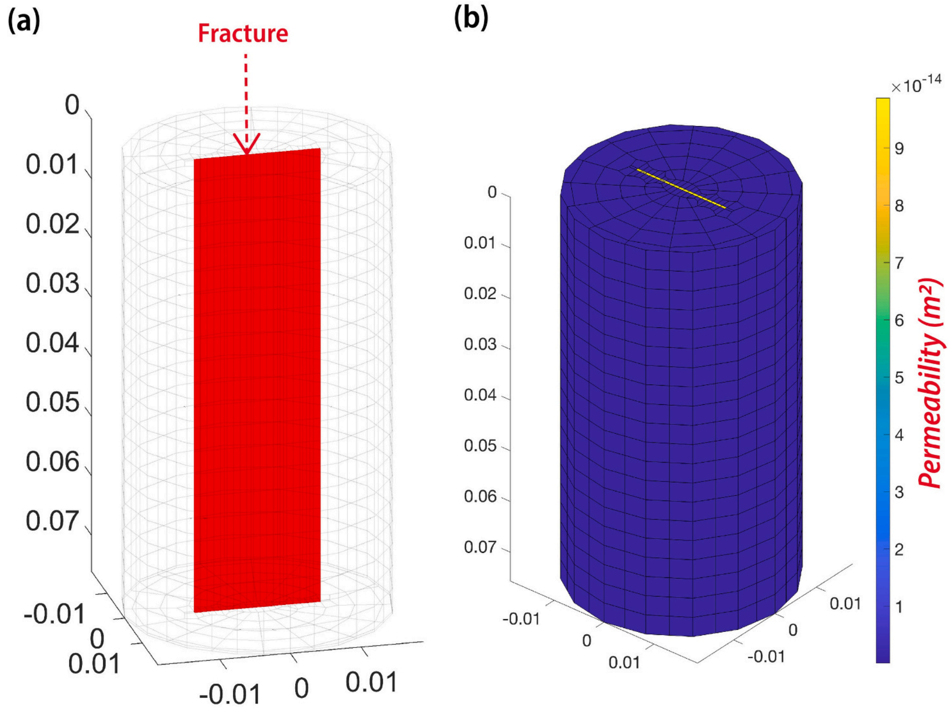

Fig. 3. Simulation domain for the core-scale BIMP numerical model. The red plane represents the fracture. (For interpretation of the references to color in this figure legend, the reader is referred to the web version of this article.)

Table 1
Outline of limestone sample model parameters.

Input data	Value	Unit
Porosity	0.07476	
Permeability	1.974×10^{-17}	m^2
Sample radius	3	in
Sample height	1.5	in
Fracture porosity	0.3494	
Fracture permeability	1.48×10^{-14}	m^2
Water viscosity	2.535×10^{-4}	Pa-s
Water density	1045	kg/m^3
Density (biofilm)	35	kg/m^3
Density (calcite)	2710	kg/m^3
Detachment rate	2.6×10^{-10}	m/Pa-s
Diffusion coefficient (microbes)	2.1×10^{-9}	m^2/s
Diffusion coefficient (oxygen)	2.32×10^{-9}	m^2/s
Diffusion coefficient (urea)	1.38×10^{-9}	m^2/s
Dispersion coefficient (longitudinal)	1.0×10^{-3}	m
Dispersion coefficient (transverse)	4.0×10^{-4}	m
Fitting factor	3	
Half-velocity constant (oxygen)	2.0×10^{-5}	kg/m^3
Half-velocity constant (urea)	21.3	kg/m^3
Maximum specific growth rate	4.17×10^{-5}	1/s
Maximum rate of urease utilization	0.0161	1/s
Microbial attachment rate	8.51×10^{-7}	1/s
Microbial death rate	3.18×10^{-7}	1/s
Yield growth coefficient	0.5	
Yield coefficient (calcite/urea)	1.67	
Oxygen consumption factor	0.5	
Critical porosity	0.1	
Minimum permeability	1.0×10^{-20}	m^2
Residual water saturation	0.27	
Treatment injection rate	8.33×10^{-10}	m^3/s
Molarity of microbe solution	0.3	mol/m^3
Molarity of oxygen solution	0.03	mol/m^3
Molarity of urea solution	60	mol/m^3
Water compressibility	4.6×10^{-10}	1/Pa
Rock compressibility	8.0×10^{-10}	1/Pa

at a steady state.

Fig. 5a–c presents the molar concentrations of the microbes, oxygen, and urea after 24 h of injecting each at molarities of 0.3 mol/m^3, 0.03 mol/m^3, and 60 mol/m^3, respectively. The results show that the injected solutions flow primarily through the fracture and diffuse further into the matrix during injection. So, the maximum values of the molar concentrations in Fig. 5a–c are approximately equal to their corresponding injection molarities within the fracture cells. As the BIMP process continues, these three molarities decrease in the sample, as shown in Fig. S1 through S3 of the supplementary material provided. This is because the free microbes in the pores form an immobile biofilm (on the fracture face), which is regarded as a separate component in the solid phase. As the biofilm grows during oxygen injection, the concentrations of the microbes and oxygen in the pores decline.

Fig. 5d–f presents the profiles of the molar concentrations of the biofilm, calcite, and permeability after 30 days of BIMP treatment. As expected (shown in supplementary Fig. S4), the molarity of the biofilm increases from the beginning of the microbial solution injection until the beginning of the urea solution injection, where the biofilm molarity starts to decline, as the microbes die after reacting with urea to produce calcites. This is consistent with the increase in the molarity of the calcite (shown in Fig. S5) from the beginning of the urea solution injection until the end of the BIMP treatment. These calcites plug the void spaces in the fracture, leading to a reduction in the permeability of the sample. In addition to our calculation of the average permeability of the entire sample discussed in the next subsection, we also computed the evolution of the permeability in all simulation cells. The permeability at the end of the BIMP treatment is shown in Fig. 5f. The results show that the permeability decreases from the beginning of the urea solution injection to the end of the BIMP treatment. A comparison of the permeability before treatment (in Fig. 3b) to the permeability after treatment (in Fig. 5f) shows that the permeability in both the matrix and fracture decreases by an order of magnitude.

4.2. Comparison of the limestone core-scale simulation to experimental data

Considering that the experimental procedure discussed in this work yields the entire sample permeability before and after the BIMP treatment, we need a procedure to estimate an average permeability from the core-scale simulation performed. Using a simple volume-weighted or harmonic averaging of the permeability of all the cells in the simulation domain could yield misleading results. This is because although a series averaging scheme applies to cells vertically on top of each other, it does not apply to cells in the same layer, which could be fracture or matrix cells. To accurately estimate the average permeability of the entire sample, we simulated single-phase water flow at a constant rate through the core for 24 h before and after the BIMP treatment. The idea is to obtain steady-state flow through the sample and extract the drop in potential ($\Delta\Phi$) across the sample from the numerical simulation model. The sample permeability is then calculated by making permeability the subject of the Darcy flow equation as follows:

$$K = \frac{q\,\mu\,h}{A\,(\Delta P - \rho g h)}, \tag{19}$$

where K, A, and h refer to the sample's permeability, cross-sectional area, and height, whereas q and μ refer to the constant flow rate and viscosity of the water flowing through the sample.

Although most of the parameters in Eq. (19) are readily available from our simulation model, it is challenging to accurately estimate the pressure drop (ΔP) across the sample. The pressure at the top face of the sample was specified, but the fluids were injected into a thin bottom layer at a [39] rate. The bottom layer was made very thin and set to a high permeability value (same as the fracture permeability) to facilitate fluid injection without affecting the total fluid storage in the sample. Therefore, the bottom pressure to be used in estimating ΔP should be an average of the pressure in the layer above this thin bottom layer. The obvious averaging scheme to estimate this average pressure is volume-

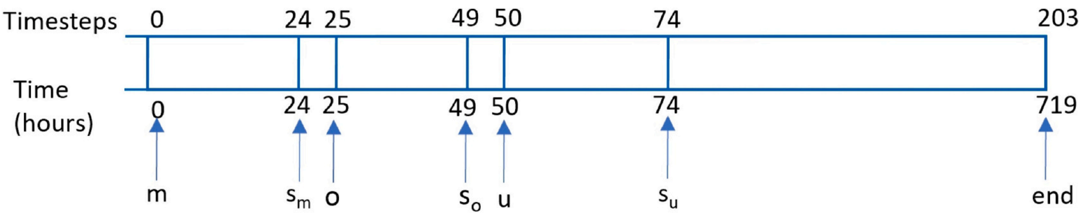

Fig. 4. Summary of the treatment schedule for one phase of microbe, oxygen, and urea solution injection. We first injected the microbes at a molarity (or molar concentration) of 0.3 mol/m^3 for 24 h. We stopped injecting for 1 h to connect the core flooding setup to the oxygen supply. Next, we injected oxygen at a molar concentration of 0.03 mol/m^3 for 24 h and paused the injection for another hour. The oxygen facilitates the growth of the microbes in the sample. Next, we injected the urea dissolved in water at a molar concentration of 0.03 mol/m^3 for 24 h and left the system to react for 30 days. It is worth mentioning that fluid solutions containing the specified molarities of microbes, oxygen, and urea were injected at the constant injection rate of 8.3 × 10^{-10} m^3/s, as in Table 1.

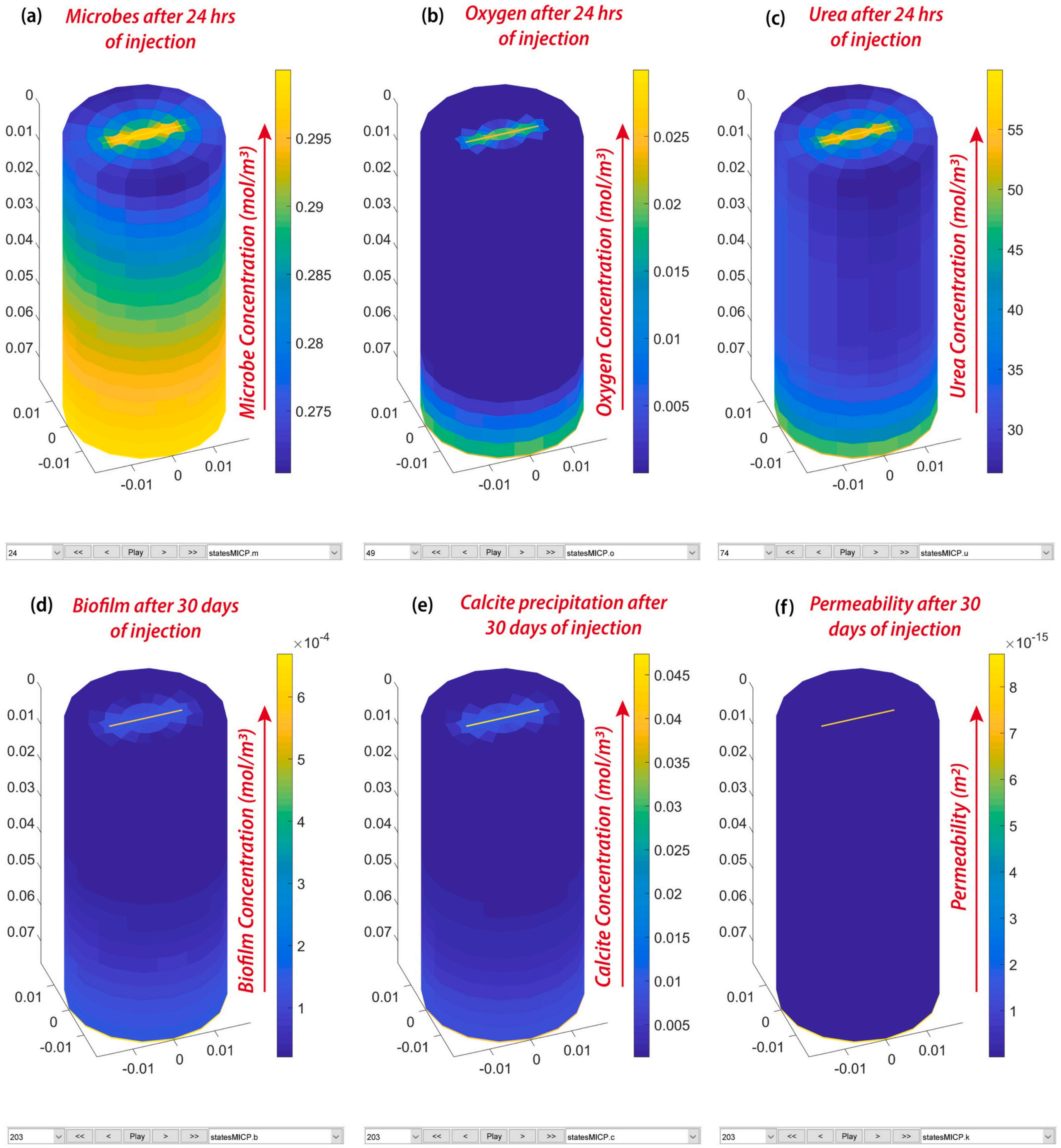

Fig. 5. The profiles on the first row show the molar concentrations of the (a) microbes, (b) oxygen, and (c) urea after 24 h of injecting them at molar concentrations of 0.3 mol/m^3, 0.03 mol/m^3, and 60 mol/m^3, respectively. The profiles on the second row show the molar concentrations of the (d) biofilm, (e) calcite, and (f) permeability after 30 days of BIMP treatment.

weighted averaging. However, this scheme will exaggerate the contribution of the matrix cells to the average pressure because they are more in number and larger in size when compared to the fracture cells in each layer. In a relentless pursuit to obtain a very accurate estimate of the average pressure for this penultimate layer, we used the "flow diagnostics" module in MRST to estimate the total time of flight (TOF) for each cell in the domain. We then extracted the TOF for the bottom layers and inverted them to obtain an inverse TOF, which indicates the flow velocity through these cells. The inverse TOF is used as the weighting factor to estimate the average pressure (p^b_{avg}) in the penultimate layer as follows:

$$p^b_{avg} = \frac{\sum_{i=1}^{n_{cp}} P_i * TOF_i^{-1}}{\sum_{i=1}^{n_{cp}} TOF_i^{-1}}, \tag{20}$$

where P_i and TOF_i^{-1} represent the pressure and inverse time of flight in each cell *i*. Having estimated ΔP from the difference between p_{avg}^{b} and the top face pressure, which is maintained at the initial pressure value, Eq. (19) is used to estimate the permeability based on the single-phase water injection experiment simulated before the BIMP treatment. After the BIMP treatment, we use the post-treatment permeability and porosity values for all grid blocks to simulate a second single-phase water injection for estimating the post-treatment sample permeability. To ensure that the BIMP treatment does not seal the thin layer at the bottom, we manually reset its permeability to its pre-treatment value. Using this procedure, we obtained sample permeability values of 14.37×10^{-2} mD and 8.38×10^{-2} mD before and after the BIMP treatment, respectively. This implies a sample permeability reduction of ~42 %, which matches our experimental permeability reduction of 44 % (with an accuracy of 95 %) without calibrating the BIMP model parameters in Landa-Marbán et al. [36].

To decide the optimum mesh size used in Section 4, we iteratively refined the mesh for the limestone core in the Z-direction and estimated the permeability before and after the BIMP treatment. Table 2 and Fig. 6 summarize our mesh sensitivity result for the core-scale model validated against the experimental data. There were ten layers in the 588-cell mesh summarized in the first row of Table 2. All subsequent rows had two times more layers than the previous one. It is worth mentioning that a mesh refinement in the other directions does not result in clear, systematic, and converging trends in the permeability like that shown in Fig. 6. This is consistent with the permeability calculations being based on flow in the direction of the Z-axis. Considering the focus on permeability in the BIMP treatment, the 3003-cell mesh used in the paper appears to be optimum because the permeability before and after treatment does not reduce much further at finer resolutions. These mesh sensitivity studies have been included in our supplementary information to maintain the focus on the experimental validation and application of the BIMP treatment in the manuscript. The next section discusses the application of the BIMP process to curtail CO_2 and hydrogen leakage at the field scale.

5. Field application of BIMP for long-term green energy security in geologic formations

This section presents the application of BIMP for curtailing the leakage of CO_2 and hydrogen through naturally fractured caprocks. In the first subsection, we start with a simulation study of the BIMP treatment of a realistic fractured reservoir for one month. By simulating a 30-day injection of CO_2 and hydrogen before and after the BIMP treatment, we evaluate the geologic formation's potential for the short-term storage of CO_2 and hydrogen in the next two subsections. Finally, the last subsection discusses our simulation of the injection of these gases for up to 1100 years (in the case of CO_2 storage) to quantify gas storage efficiency as a function of the amount of gas that leaks through the treated fractured rock. This is important considering the potential environmental consequence of even a slow leakage of CO_2 or hydrogen into shallower drinking water sources.

5.1. Field-scale study of the BIMP treatment of a fractured formation

The technological concept presented in this work involves performing three phases of BIMP treatment through a horizontal well, which is close and parallel to the cap rock in the formation to be treated. The BIMP model parameters presented in Section 4 were also used in this section. However, the rates and concentrations of the injected microbes, oxygen, and urea were modified in the field-scale applications discussed in the following three subsections. The system used to assess CO_2 and hydrogen leakage consists of two limestone storage rocks separated by a naturally fractured shale caprock. Each of these formations is meshed with three layers of unstructured grids with unequal thickness in the z-direction, as shown in Fig. 7(a).

In the 16,245-cell mesh for the simulation domain shown in Fig. 7a, the fracture cells belonging to each fracture plane are colored differently. These fractures start at the top of the lower limestone unit and end at the bottom of the upper limestone unit. The blue horizontal well is used for the BIMP treatment, whereas the red vertical well is used for CO_2 or hydrogen injection before and after the BIMP treatment. The idea behind injecting these gases before and after three phases of BIMP treatment is to evaluate the leakage rate of these gases before and after BIMP treatment. Fig. 7b presents the X-Y view of the simulation domain, which shows the location of the natural fractures relative to the well location. Table 3 summarizes the other model parameters used in this field-scale BIMP simulation and the corresponding injection conditions for the GCS and GHS simulations before and after the BIMP treatment. Unlike the 1.5′ diameter and 3″ long score samples used in the laboratory experiments, the reservoir studied in the rest of this research is 200 m × 175 m × 70 m. So, several model parameters, such as the injection duration and injected fluid volumes, are much larger in the field-scale problem to meaningfully treat the fractures in this geologic formation. Other model parameters not provided in Table 3 are the same as in Table 1.

The result in Fig. 8a shows the maximum molar concentrations in the fractures during the first phase of the BIMP treatment, where microbes were injected at a concentration of 0.3 mol/m^3 for 15 h. It indicates that although the injected microbes got into the fractures closest to the injection well, the concentrations of these microbes in the fractures varied. Similarly, the result in Fig. 8b–c shows the maximum molar concentrations during oxygen and urea injection at concentrations of 0.06 and 30 mol/m^3 for 5 and 9 days, respectively. After this first phase of BIMP treatment, the biofilm and calcite concentrations in the fractures grew from zero to the values shown in Fig. 8d–e. This growth of the biofilm and calcite concentrations reduced the permeability (of the fractures near the injector) from their initial values of 10 Darcy to the values shown in Fig. 8f. To quantify and summarize the degree of the fracture treatment after phase 1, we computed the percentage reduction in the average permeability of all the fractures relative to the initial average fracture permeability. It showed a 7.4 % reduction in the average fracture permeability.

The second phase of BIMP treatment involved injecting the microbes, oxygen, and urea at concentrations of 0.3, 0.03, and 30 mol/m^3 for 15, 60, and 40 h, respectively. Fig. 9a–c shows their concentrations after this treatment phase. These images show a reduction in the concentration of the microbes, which can be attributed to the depletion of the microbes during the first phase of the BIMP treatment and the reduced molarity of the microbes during this second phase of BIMP treatment. Fig. 9d–e shows the biofilm and calcite concentrations at the end of phase 2 of the treatment. Although the concentrations in the most affected fractures do not appear visibly different than those in Fig. 9d–e, a close inspection of the fractures on the left of the images shows that some more fractures were affected by this phase of BIMP treatment. These newly treated fractures can be more easily identified by comparing Figs. 8f to 9f. We also computed the percentage reduction in the average permeability of all the fractures after phase 2 compared to the initial average fracture permeability. It showed a 9.2 % reduction in the average fracture permeability.

In the third and final phase of the BIMP treatment, we injected oxygen at 0.04 mol/m^3 for 30 h and shut in the well for 10 h. Next, we injected urea at a concentration of 15 mol/m^3 for 40 h, after which the

Table 2
Summary of mesh sensitivity results.

# of cells	K before BIMP (mD)	K after BIMP (mD)	Reduction
588	0.344	0.209	39.28 %
1243	0.168	0.098	41.21 %
3003	0.144	0.084	41.65 %
8323	0.145	0.084	42.16 %
26,163	0.146	0.084	42.16 %

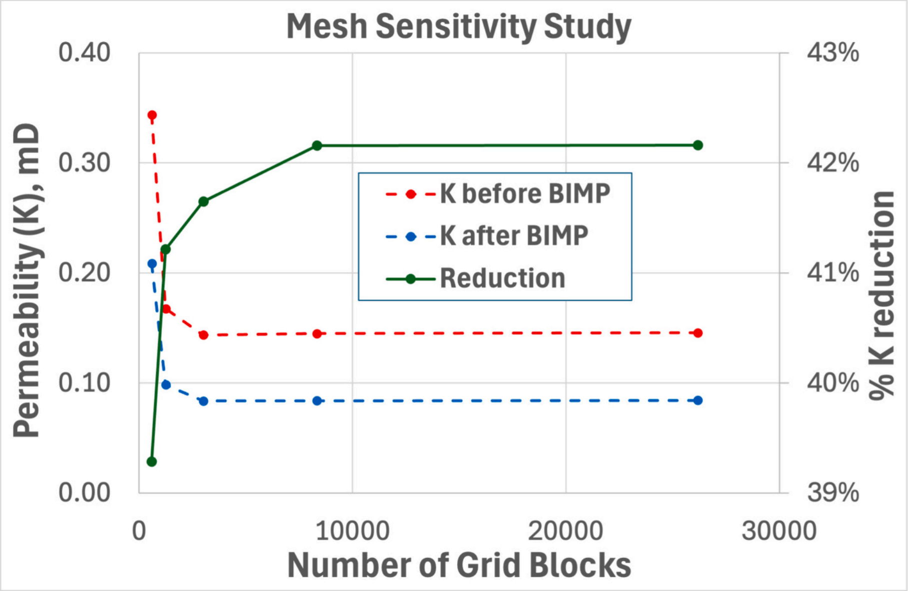

Fig. 6. Plots show that the permeability before and after treatment converges to ~0.144 and ~0.084 mD when the number of cells is 3003.

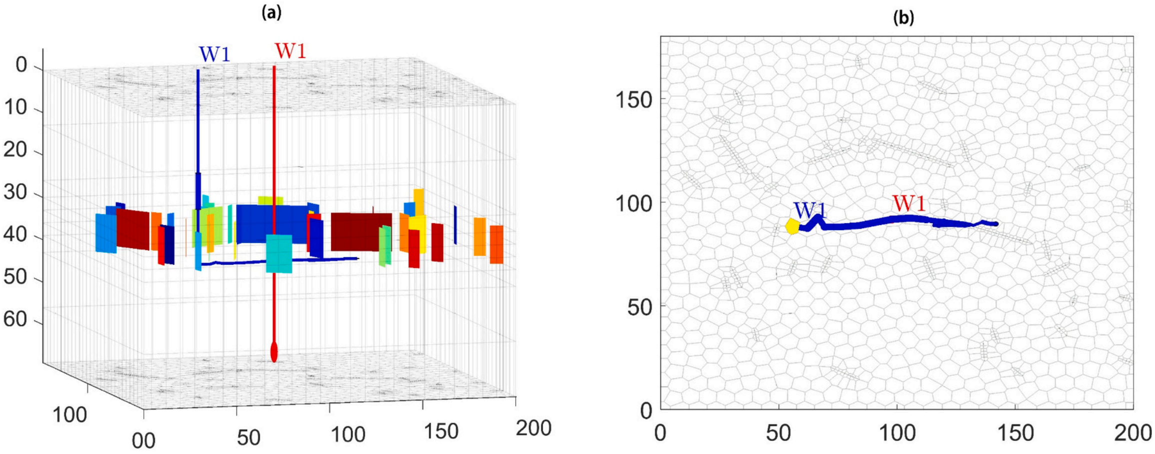

Fig. 7. (a) shows the 3D view of the simulation domain for the field-scale BIMP numerical model, whereas (b) shows its X-Y view. The color of the fracture cells indicates the natural fracture planes they belong to. (For interpretation of the references to color in this figure legend, the reader is referred to the web version of this article.)

well was shut in for 25 h. The result in Fig. 10a–b shows the maximum oxygen and urea concentrations after this treatment phase. Fig. 10c–e shows the biofilm and calcite concentrations and fracture permeability at the end of phase 3 of the BIMP treatment. Comparing Figs. 10e to 9f, we observe that the treated fractures to the left of the domain have been treated further and show a further reduction in fracture permeability. We also computed the percentage reduction in the average permeability of all the fractures after phase 3 in comparison to the initial average fracture permeability. It showed a 10.1 % reduction in the average fracture permeability.

One of the unique features of this work compared to previous simulations of BIMP is the relentless efforts to ensure that the flowing bottomhole pressure stays only slightly higher than the initial reservoir pressure. To this end, we carefully selected the fluid injection rates, duration, and molarities. Furthermore, we simulated water production from the well annulus in the limestone formation above the fractured shale layer during phases 2 and 3 of the BIMP treatment. These rates and flowing bottomhole pressures are plotted in Fig. 11a–c. The water production from the upper limestone formation could also explain the BIMP treatment of some of the natural fractures on the left side of the domain after phases 2 and 3. Finally, Fig. 11d explicitly shows the extent to which each of the 40 natural fracture (NF) planes in the storage reservoir are treated after each phase of the BIMP treatment. The best-treated fractures are those closest to the horizontal treatment well in the reservoir, and they show up to 100 % reduction in the average fracture permeability. In contrast, the natural fractures furthest from the horizontal well do not show any natural fracture permeability reduction because additional wells will be needed to treat those.

5.2. *Field-scale application of BIMP for short-term geologic CO_2 storage*

To evaluate the field-scale application of BIMP in curtailing the leakage of CO_2 through a naturally fractured caprock, we simulated CO_2 injection at 1.5×10^{-5} m^3/day into the red-colored well in Fig. 7. First, we simulated CO_2 injection for 30 days before the three-stage BIMP treatment and obtained the CO_2 saturation profile presented in Fig. 12a. Next, we performed the BIMP treatment, as discussed in the previous section, and injected CO_2 at the same rate for 30 days. The resulting CO_2 saturation at the end of the simulation is shown in Fig. 12b. Comparing the CO_2 saturation profiles before and after the BIMP treatment, we

Table 3
Outline of field-scale model parameters.

Input data	Value	Unit
Limestone porosity	0.15	
Limestone permeability	2.0×10^{-14}	m^2
Fracture porosity	0.60	
Fracture permeability	2.0×10^{-11}	m^2
Shale porosity	0.0541	
Shale permeability	9.87×10^{-21}	m^2
Number of fractures	40	
Water viscosity	2.535×10^{-4}	Pa-s
Water density	1045	kg/m^3
Residual water saturation	0.27	
Critical gas saturation	0.20	
Well radius	15	cm
Horizontal well length	90	m
CO_2 reference pressure	12.82	MPa
CO_2 reference temperature	343.15	K
CO_2 Injection rate	1.73	m^3/s
Hydrogen reference pressure	12.82	MPa
Hydrogen reference temperature	343.15	K
Hydrogen Injection rate	1.73	m^3/s

observe that a few of the natural fractures that CO_2 leaked through in Fig. 12a no longer serve as CO_2 leakage paths in Fig. 12b because they were sealed during the BIMP treatment. This is shown by the replacement of the warmer colors in those fractures with blue in Fig. 12b.

All the caprock cells in the middle layer of the domain were removed to show the CO_2 gas saturation profile in Fig. 12c–e. In contrast, we obtained a clearer presentation of the CO_2 saturation profile shown in Fig. 12c–d by removing all the matrix cells in the domain. The results show that some of the fractures close to the middle to right portion of the domain were sealed during the BIMP treatment. To quantify the extent of the sealing of these fractures, we extracted the flow rate from the top of the lower limestone reservoir into the bottom face of each fracture cell in contact with it. We then summed up the rates for all fracture cells belonging to each natural fracture plane to obtain the leakage rate across each one. Unfortunately, these rates are not only a function of the distance of the fracture planes to the injection well because some fractures are larger than others, and larger fractures have higher leakage rates. To address this, we normalized the leakage rate through each fracture plane by its maximum leakage rate over the 30 days of CO_2 injection. These normalized rates were calculated before and after the BIMP treatment and the values for the four best-treated fracture planes are plotted in Fig. 12e. The results show that there is no leakage through fracture #1 after the BIMP treatment, there is an insignificant leakage only towards the end of the simulation period after treating fracture #6, and fractures #30 and #27 have a significant CO_2 leakage reduction after the BIMP treatment.

5.3. Field-scale application of BIMP for short-term geologic hydrogen storage

This section focuses on the application of the BIMP treatment to mitigate hydrogen leakage instead of CO_2 leakage. So, we simulated 30 days of hydrogen injection at the same injection rate into the same simulation domain before and after an identical BIMP treatment. Fig. 13a–b shows the hydrogen saturation after 30 days of hydrogen injection into the reservoir before and after BIMP treatment. A comparison of these two hydrogen saturations indicates that the BIMP process sealed the annotated fractures. Compared to the CO_2 saturation profiles shown in Fig. 12a–b, Fig. 13a–b shows that the hydrogen plume covers a broader area of the top layer of the lower limestone formation. This is expected because hydrogen is lighter and more mobile than CO_2.

As in Fig. 12c–d, Fig. 13c–d clearly shows the hydrogen saturation profile in the fractures by removing all matrix cells in the simulation domain. Comparing these two images shows the treated fractures in blue. The same approach used in Fig. 12e is used to compute the normalized hydrogen leakage rates before and after the BIMP treatment, shown in Fig. 13e. The results show that the best-treated fracture (fracture #1) is completely sealed, whereas the other fractures are sealed to different degrees. It is worth noting that the fracture

(a) Microbes during phase 1 BIMP treatment (b) Oxygen during phase 1 BIMP treatment (c) Urea during phase 1 BIMP treatment

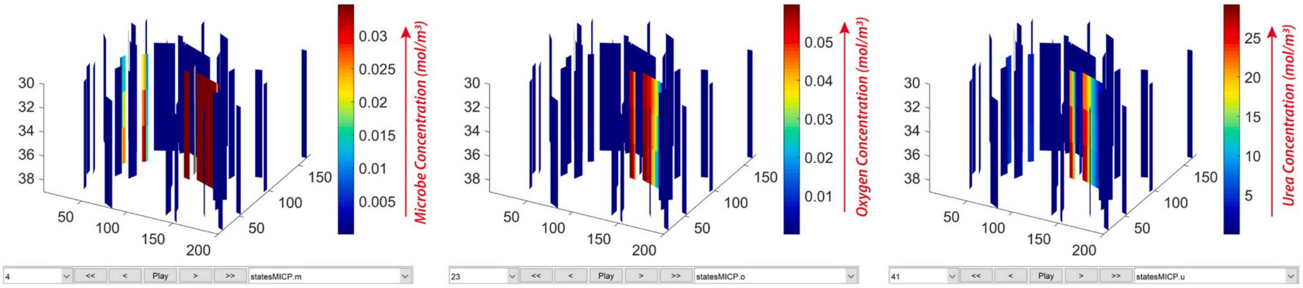

(d) Biofilm at end of phase 1 BIMP treatment (e) Calcite precipitation at end of phase 1 BIMP treatment (f) Permeability at end of phase 1 BIMP treatment

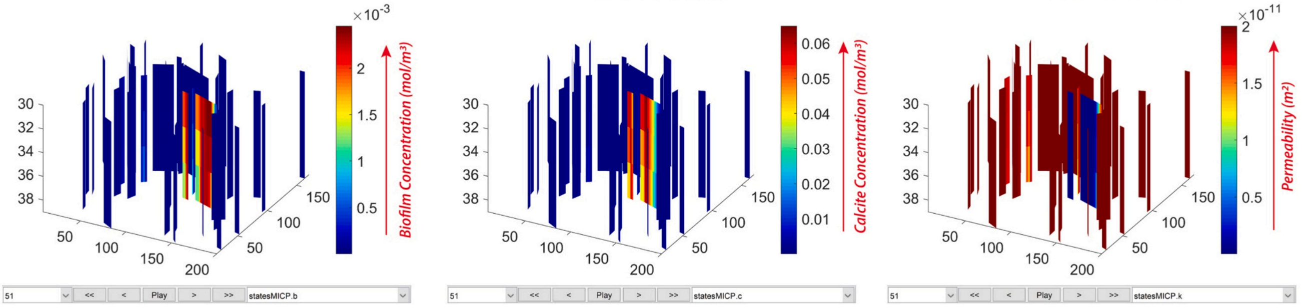

Fig. 8. The profiles on the first row show the maximum molar concentrations of the (a) microbes, (b) oxygen, and (c) urea after injecting them at molar concentrations of 0.3, 0.06, and 30 mol/m^3 during phase 1 of BIMP treatment. The second row shows the molar concentrations of the (d) biofilm, (e) calcite, and (f) permeability at the end of phase 1 of BIMP treatment.

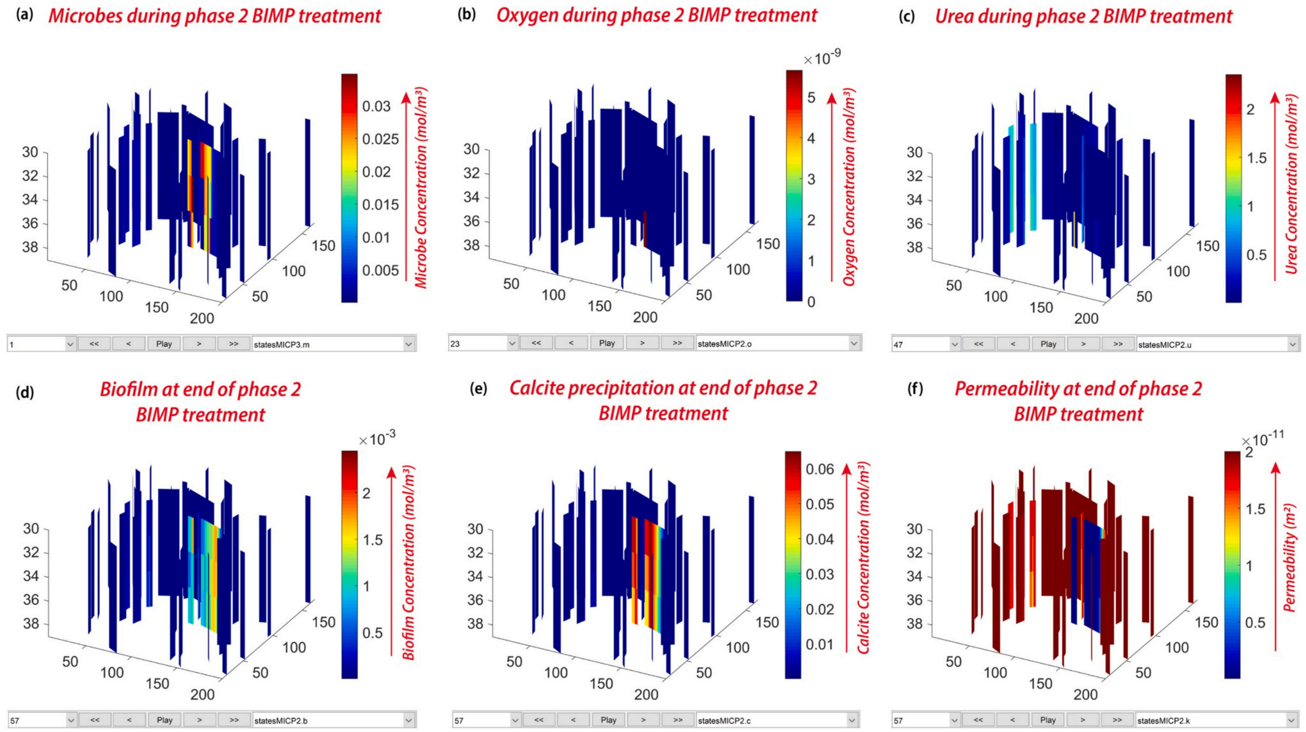

Fig. 9. The profiles on the first row show the maximum molar concentrations of the (a) microbes, (b) oxygen, and (c) urea after injecting them at molar concentrations of 0.3, 0.03, and 30 mol/m^3 during phase 2 of BIMP treatment. The second row shows the molar concentrations of the (d) biofilm, (e) calcite, and (f) permeability at the end of phase 2 of BIMP treatment.

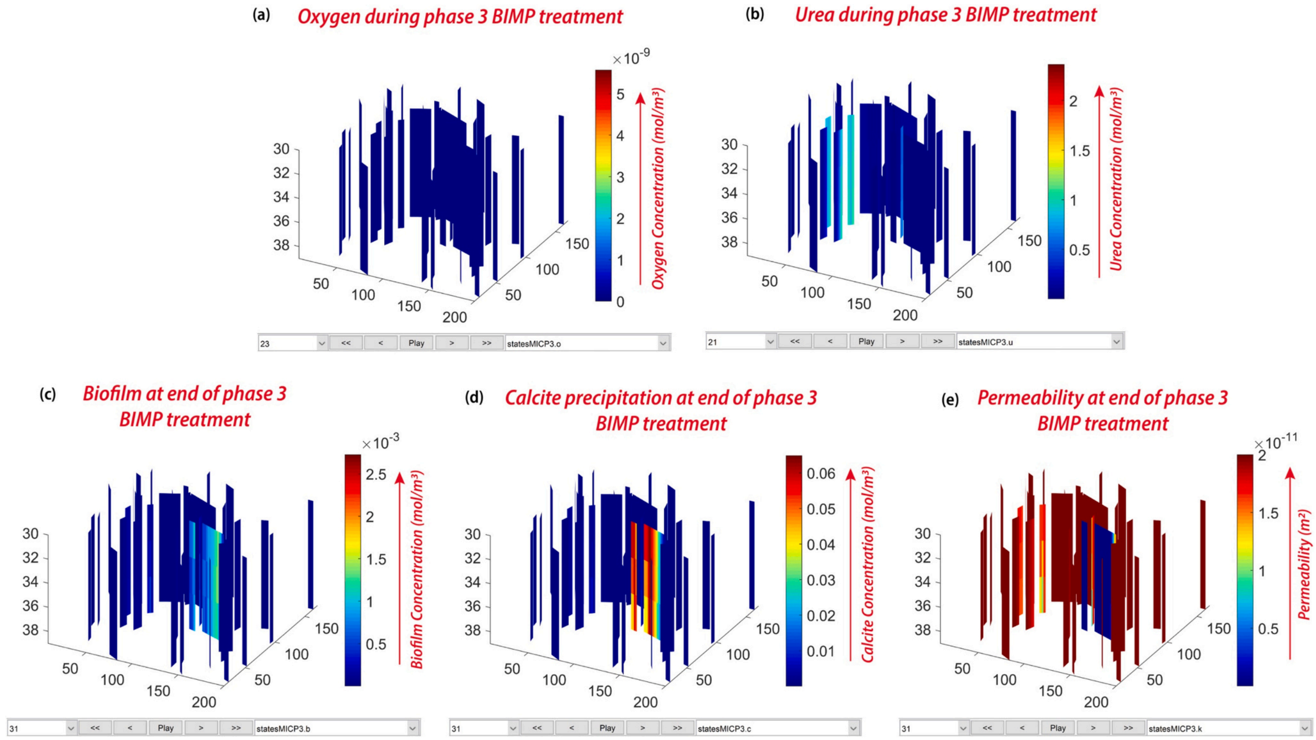

Fig. 10. The profiles on the first row show the maximum molar concentrations of (a) oxygen and (b) urea after injecting only oxygen and urea at molar concentrations of 0.04 and 15 mol/m^3 during phase 3 of the BIMP treatment. The second row shows the molar concentrations of the (c) biofilm, (d) calcite, and (e) permeability at the end of phase 3 of BIMP treatment.

permeabilities do not become zero after treatment. So, in comparison to the CO_2 leakage rates, the higher hydrogen leakage rates observed after treatment are consistent with higher mobility of hydrogen in comparison to CO_2.

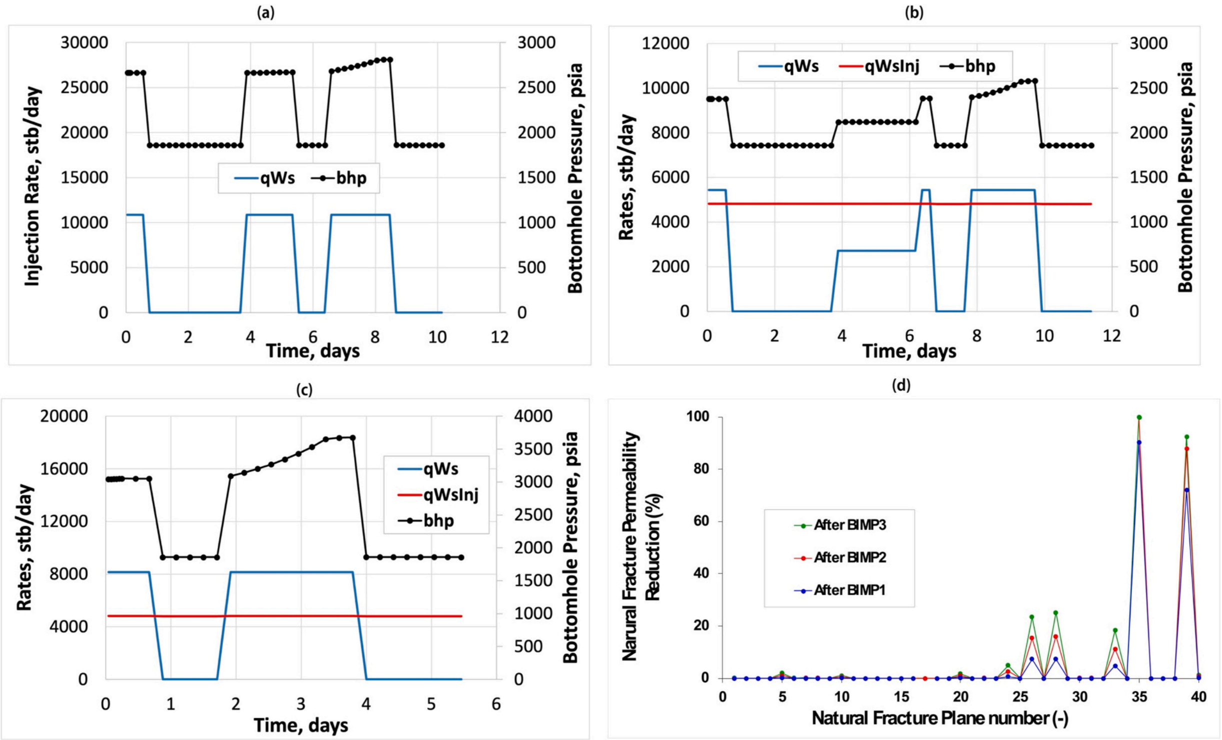

Fig. 11. Images show the injection performance results after (a) phase 1, (b) phase 2, and (c) phase 3 of the BIMP treatment. The results in (d) show the percentage reduction in the natural fracture permeability for each of the 40 natural fractures in the simulation domain.

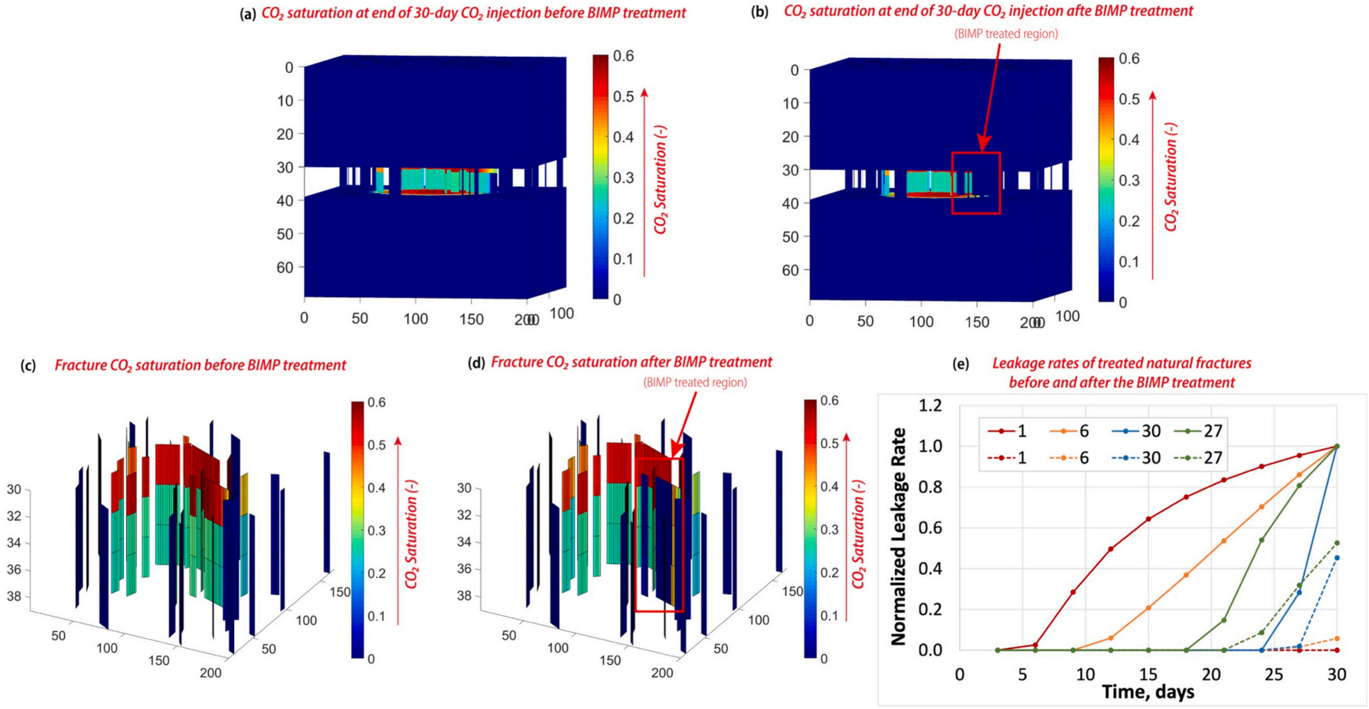

Fig. 12. The results on the first row show the CO_2 saturation profile at the end of the 30-day CO_2 injection (a) before and (b) after the BIMP treatment. The results on the second row show (c) fracture CO_2 saturation before BIMP treatment, (d) fracture CO_2 saturation after BIMP treatment, and (e) normalized leakage rate of some of the best-treated natural fractures before and after the BIMP treatment. The fractures in the circled region were sealed during the BIMP treatment. (For interpretation of the references to color in this figure, the reader is referred to the web version of this article.)

5.4. Estimation of storage efficiency for long-term geo-energy storage

Having demonstrated the near-term potential of curtailing CO_2 leakage using BIMP by simulating 30 days of CO_2 and hydrogen treatment, this section focuses on evaluating the gas storage efficiency for long-term GCS and for 25 years of cyclic hydrogen storage and

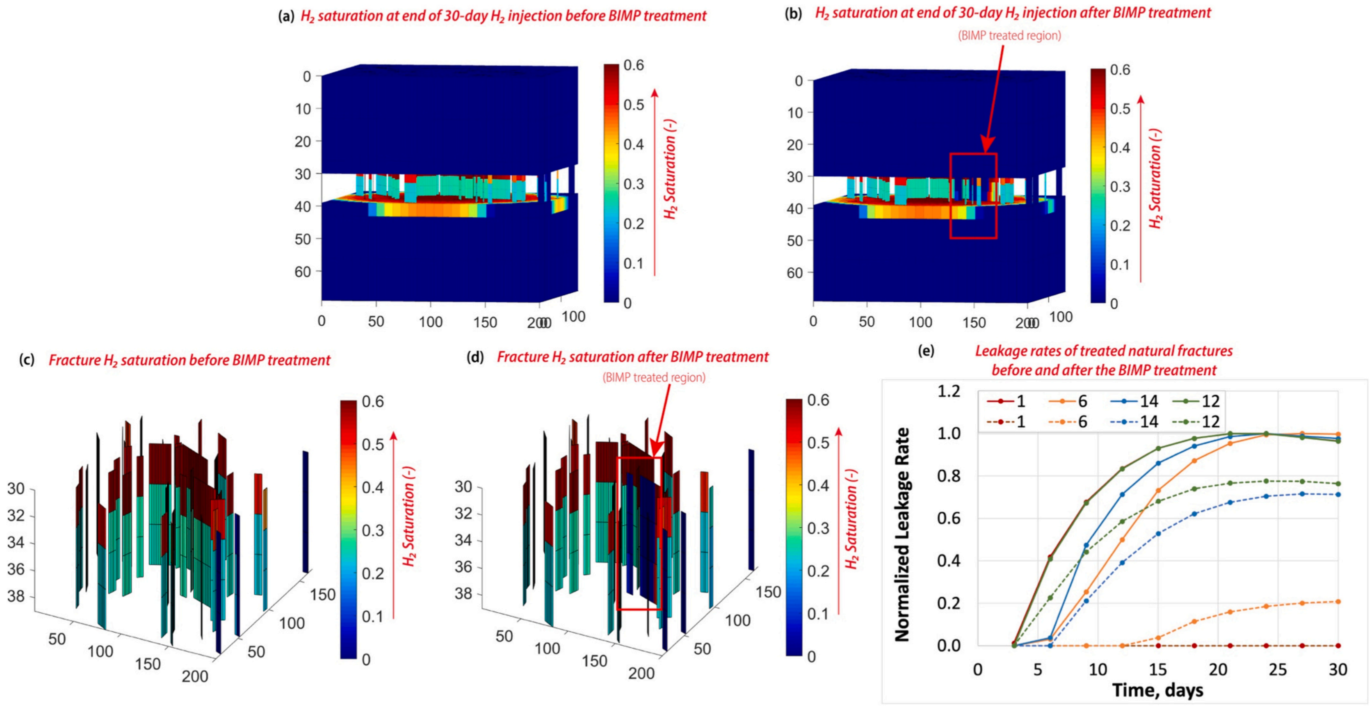

Fig. 13. The results on the first row show the hydrogen saturation profile at the end of the 30-day hydrogen injection (a) before and (b) after the BIMP treatment. The results on the second row show (c) fracture H_2 saturation before BIMP treatment, (d) fracture H_2 saturation after BIMP treatment, and (e) normalized leakage rate of some of the best-treated natural fractures before and after the BIMP treatment. The fractures in the circled region were sealed during the BIMP treatment.

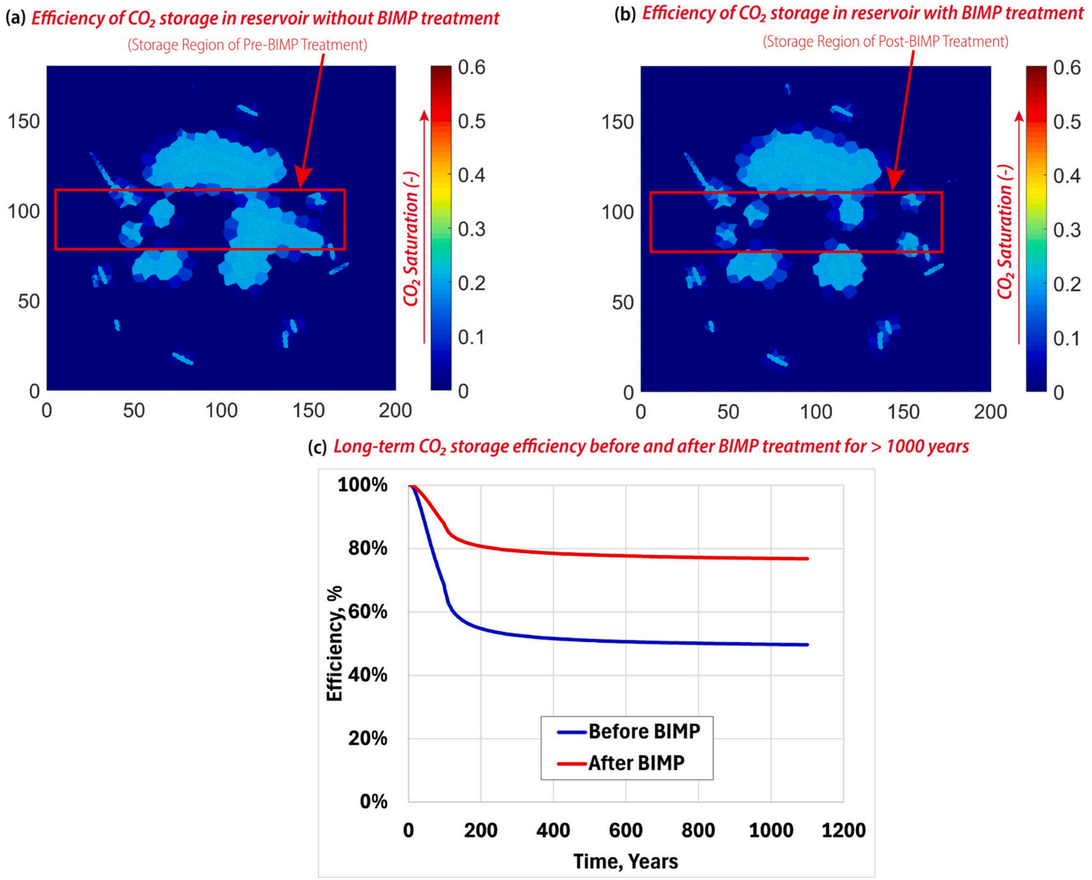

Fig. 14. The results show (a) the CO_2 saturation profiles in the top layer of the simulation domain before BIMP treatment, (b) the CO_2 saturation profiles in the top layer after BIMP treatment, and (c) the plot of storage efficiency for the red boxed region before and after BIMP treatment. (For interpretation of the references to color in this figure legend, the reader is referred to the web version of this article.)

production. To this end, we simulated CO_2 injection for 100 years, followed by a period of 1000 years, where the injection is stopped, and the CO_2 plume is allowed to migrate in the reservoir. The top views of the CO_2 gas saturation profiles after 1100 years of simulation of the untreated and BIMP-treated reservoirs are presented in Fig. 14a–b. Comparing the CO_2 gas saturation in the red region before and after treatment shows that the leakage through the fractures in the BIMP-treated region is significantly reduced.

The storage efficiency is estimated as follows:

$$\text{Storage Efficiency} = 100\% - \frac{\text{Gas volume leaked at SC}}{\text{Total gas volume injected at SC}}, \tag{21}$$

where *SC* represents standard conditions of 101,325 Pa and 288.7 °F. However, considering that one well is insufficient for treating all the natural fractures in the simulation domain presented, we compute the storage efficiency for a subset of the domain in the region where the well is located. The top view of this region is highlighted as the red rectangle in Fig. 14a–b. It runs from the top to the bottom of the simulation domain. So, the storage efficiency for this reduced reservoir portion is estimated using Eq. (21), but for the red subset of the domain. The corresponding storage efficiencies before and after BIMP treatment of this region are shown in Fig. 14c. The results show that the efficiency increases from 50 % before treatment to 77 % after BIMP treatment. Multiple horizontal wells will be needed to treat all the natural fractures in the reservoir simulation domain.

In contrast to the 30-day hydrogen storage presented in the previous section, here we studied the cyclic injection, soaking, and production of hydrogen over 25 years. The idea is to evaluate the storage efficiency over this relatively long period. In each of the 25 years, we simulated a cycle of hydrogen injection for 150 days, 65 days of shut-in, and 150 days of production. Fig. 15a shows the hydrogen gas saturation in the topmost layer after 25 years of cyclic injection/production for the untreated reservoir. In contrast, Fig. 15b shows the hydrogen gas saturation after 25 years of the cyclic injection/production for the BIMP-treated reservoir. As expected, the amount of hydrogen that leaked into the top layer is much less in the region above the well used for the BIMP treatment. The hydrogen storage efficiency is also estimated using Eq. (21), as in the long-term CO_2 storage case. Fig. 15c shows a significant improvement in the storage efficiency (at 25 years) from 65 % to 87 % after BIMP treatment. It is worth noting that although it is typical to consider injecting a cushion gas like CO_2 or nitrogen before hydrogen gas injection, the focus here is on assessing hydrogen leakage before and after treatment. So, we do not repeat this well-studied effect of cushion gases in this work. Finally, to further increase the storage efficiencies reported in this section, we could perform more phases of BIMP treatment, use more wells for the treatment, and optimize the mole fractions and injection rates of the microbes, oxygen, and urea solution.

6. Conclusions

This work presents the first core-to-field-scale experimental and numerical study of a BIMP process designed to enhance CO_2 and hydrogen storage security in subsurface rocks by sealing natural fractures in these underground formations. The core-scale simulation was validated against laboratory studies of the BIMP process to obtain the

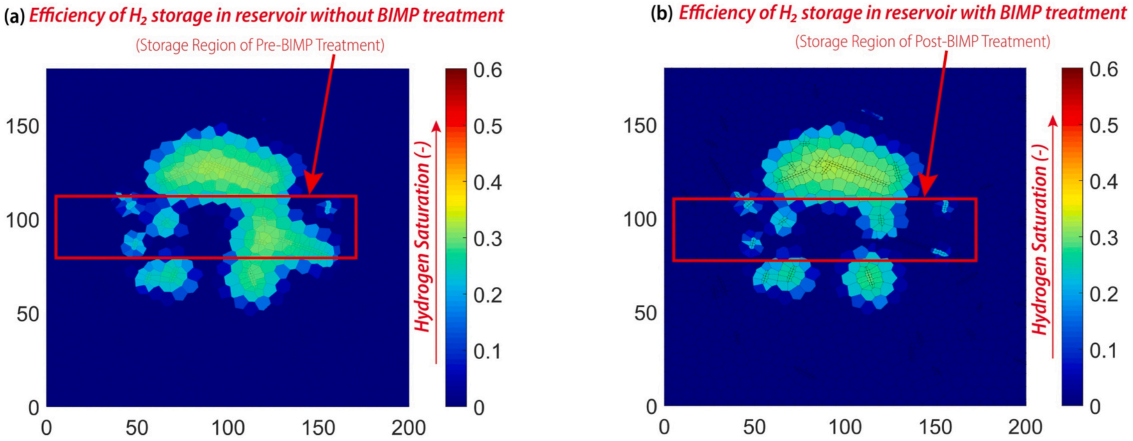
(a) Efficiency of H_2 storage in reservoir without BIMP treatment

(b) Efficiency of H_2 storage in reservoir with BIMP treatment

(c) H_2 storage efficiency before and after BIMP treatment

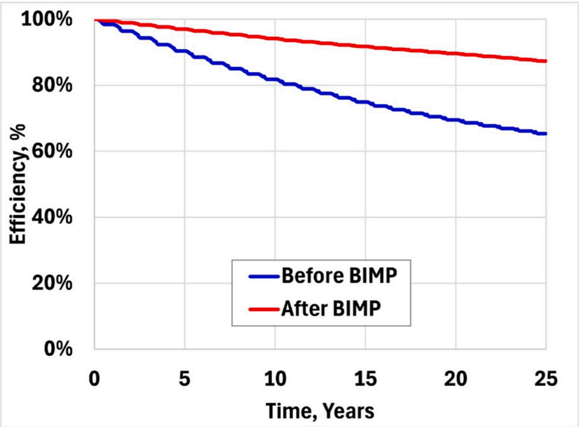

Fig. 15. The results show (a) the hydrogen saturation profiles in the top layer of the simulation domain before BIMP treatment, (b) the hydrogen saturation profiles in the top layer after BIMP treatment, and (c) the plot of storage efficiency for the red boxed region before and after BIMP treatment. (For interpretation of the references to color in this figure legend, the reader is referred to the web version of this article.)

model parameters used in field-scale studies. These model parameters were used to simulate a three-phase BIMP treatment that significantly reduced the permeability of several natural fractures. We quantified the potential leakage of CO_2 and hydrogen by injecting these gases into a porous medium with a naturally fractured caprock. The results from this work are summarized as follows:

a) We developed and validated the core-scale BIMP model against experimental data with an accuracy of 95 %.
b) The modeling of CO_2 and hydrogen injection for storage before and after the BIMP treatment showed that gas leakage could be completely sealed in some pre-existing fractures depending on their distance from the injection well.
c) More natural fractures are sealed to higher degrees with each additional phase of the BIMP process. This implies that several phases of the BIMP can be designed and optimized to seal off caprocks containing natural fractures. Thus, this work directly addresses the problem of gas leakage and security in geologic CO_2 and hydrogen storage.
d) Comparing the underground CO_2 and hydrogen leakage rates and gas saturation values over the same injection and storage period shows that hydrogen can leak through natural fractures faster than CO_2.
e) This is the first BIMP treatment model for CO_2 and hydrogen storage that accounts for the resulting flowing bottomhole pressure increases during the BIMP process. We ensured that the pressures were within ~1500 psi (10.3 MPa) above the initial reservoir pressure. This can be achieved in the field by carefully choosing the m, o, and u molarities and producing water from a shallower formation if needed.
f) Estimating the storage efficiency of CO_2 over 1100 years shows that the BIMP treatment increases the storage efficiency from 50 % to 77 %, whereas that of hydrogen (over 25 years of cyclic injection and storage) increased from 65 % to 87 % after the BIMP treatment.

CRediT authorship contribution statement

Olufemi Olorode: Writing – review & editing, Writing – original draft, Validation, Supervision, Software, Resources, Project administration, Methodology, Investigation, Formal analysis, Conceptualization. **Oladoyin Kolawole:** Writing – review & editing, Writing – original draft, Visualization, Validation, Resources, Project administration, Methodology, Investigation, Formal analysis, Data curation, Conceptualization. **Chibuzor Igweonu:** Writing – original draft, Visualization, Validation, Investigation, Data curation. **Harun Rashid:** Methodology, Investigation.

Declaration of competing interest

The authors declare that they have no known competing financial interests or personal relationships that could have appeared to influence the work reported in this paper.

Acknowledgement

The work of O.O. and C.I. were supported by the U.S. Department of Energy, Office of Science, Office of Basic Energy Sciences, Geosciences program under Award Number DE-SC0024382.

Appendix A. Supplementary data

Supplementary data to this article can be found online at https://doi.org/10.1016/j.est.2025.115474.

Data availability

Data will be made available on request.

References

[1] J. Rutqvist, C.F. Tsang, A study of caprock hydromechanical changes associated with CO_2-injection into a brine formation, Environ. Geol. 42 (2002) 296–305, https://doi.org/10.1007/s00254-001-0499-2.
[2] S. Iglauer, A.Z. Al-Yaseri, R. Rezaee, M. Lebedev, CO_2 wettability of caprocks: implications for structural storage capacity and containment security, Geophys. Res. Lett. 42 (21) (2015) 9279–9284, https://doi.org/10.1002/2015GL065787.
[3] M. Lebedev, Y. Zhang, M. Sarmadivaleh, et al., Carbon geosequestration in limestone: pore-scale dissolution and geomechanical weakening, Int. J. Greenhouse Gas Control 66 (2017) 106–119, https://doi.org/10.1016/j.ijggc.2017.09.016.
[4] J. Alcalde, S. Flude, M. Wilkinson, et al., Estimating geological CO_2 storage security to deliver on climate mitigation, Nat. Commun. 9 (2018) 2201, https://doi.org/10.1038/s41467-018-04423-1.
[5] O. Kolawole, C. Millikan, M. Kumar, I. Ispas, B. Schwartz, J. Weber, L. Badurina, B. Šegvić, Impact of microbial-rock-CO_2 interactions on containment and storage security of supercritical CO_2 in carbonates, Int. J. Greenhouse Gas Control 120 (2022) 103755, https://doi.org/10.1016/j.ijggc.2022.103755.
[6] S. Holloway, An overview of the underground disposal of carbon dioxide, Energy Convers. Manag. 38 (1997) S193–S198, https://doi.org/10.1016/S0196-8904(96)00268-3.
[7] K.S. Lackner, A guide to CO_2 sequestration, Science 300 (5626) (2003) 1677–1678, https://doi.org/10.1126/science.1079033.
[8] D.W. Duncan, E.A. Morrissey, The concept of geologic carbon sequestration, U.S. Geological Survey, 2011. https://pubs.usgs.gov/fs/2010/3122.
[9] V. Scott, S. Gilfillan, N. Markusson, H. Chalmers, R.S. Haszeldine, Last chance for carbon capture and storage, Nat. Clim. Chang. 3 (2012) 105–111, https://doi.org/10.1038/nclimate1695.
[10] M. Bui, N.M. Dowell (Eds.), Carbon Capture and Storage, Royal Society of Chemistry, London, UK, 2019, https://doi.org/10.1039/9781788012744.
[11] S. Krevor, M. Blunt, J. Trusler, S. De Simone, An introduction to subsurface CO_2 storage carbon capture and storage, in: M. Bui, N.M. Dowell (Eds.), Carbon Capture and Storage, Royal Society of Chemistry, 2019, pp. 238–295, https://doi.org/10.1039/9781788012744-00238.
[12] R. Gholami, A. Raza, S. Iglauer, Leakage risk assessment of a CO_2 storage site: a review, Earth Sci. Rev. (2021) 103849, https://doi.org/10.1016/j.earscirev.2021.103849.
[13] P. Kelemen, S.M. Benson, H. Pilorgé, P. Psarras, J. Wilcox, An overview of the status and challenges of CO_2 storage in minerals and geological formations, Front. Clim. 1 (2019). https://www.frontiersin.org/article/10.3389/fclim.2019.00009.
[14] National Academies of Sciences Engineering Medicine, Negative Emissions Technologies and Reliable Sequestration: A Research Agenda, The National Academies Press, Washington, DC, 2019, https://doi.org/10.17226/25259.
[15] O. Kolawole, I. Ispas, M. Kumar, J. Weber, B. Zhao, G. Zanoni, How can biogeomechanical alterations in shales impact caprock integrity and CO_2 storage? Fuel 291 (2021) 120149 https://doi.org/10.1016/j.fuel.2021.120149.
[16] O. Ozotta, M. Ostadhassan, K. Liu, B. Liu, O. Kolawole, F. Hadavimoghaddam, Reassessment of CO_2 sequestration in tight reservoirs and associated formations, J. Pet. Sci. Eng. 206 (2021) 109071, https://doi.org/10.1016/j.petrol.2021.109071.
[17] O. Ozotta, O. Kolawole, M.L. Malki, T. Ore, T. Gentzis, H. Fowler, K. Liu, M. Ostadhassan, Nano- to macro-scale structural, mineralogical, and mechanical alterations in a shale reservoir induced by exposure to supercritical CO_2, Appl. Energy 326 (2022) 120051, https://doi.org/10.1016/j.apenergy.2022.120051.
[18] S. Bachu, Sequestration of CO_2 in geological media: criteria and approaches for site selection in response to climate change, Energy Convers. Manag. 41 (2000) 953–970, https://doi.org/10.1016/S0196-8904(99)00149-1.
[19] IPCC, in: B. Metz, O. Davidson, P. Bosch, R. Dave, L. Meyer (Eds.), Climate Change 2007: Mitigation of Climate Change: Contribution of Working III to the Fourth Assessment Report of the Intergovernmental Panel on Climate Change, Cambridge University Press, Cambridge, United Kingdom and New York, United States, 2007.
[20] IPCC, Climate change 2014: synthesis report, in: Core Writing Team, R.K. Pachauri, L.A. Meyer (Eds.), Contribution of Working Groups I, II and III to the Fifth Assessment Report of the Intergovernmental Panel on Climate Change, IPCC, Geneva, Switzerland, 2014 (151 pp.).
[21] IPCC, Climate change 2021: the physical science basis, in: Masson-Delmotte, et al. (Eds.), Contribution of Working Group I to the Sixth Assessment Report of the Intergovernmental Panel on Climate Change, Cambridge University Press, 2021.
[22] L. Van Der Meer, The CO_2 storage efficiency of aquifers, Energy Convers. Manag. 36 (6–9) (1995) 513–518, https://doi.org/10.1016/0196-8904(95)00056-j.
[23] S. Bachu, Review of CO_2 storage efficiency in deep saline aquifers, Int. J. Greenhouse Gas Control 40 (2015) 188–202, https://doi.org/10.1016/j.ijggc.2015.01.007.
[24] R. Tarkowski, Underground hydrogen storage: characteristics and prospects, Renew. Sust. Energ. Rev. 105 (2019) 86–94, https://doi.org/10.1016/j.rser.2019.01.051.
[25] N.S. Muhammed, B. Haq, D.A. Shehri, A. Al-Ahmed, M.M. Rahman, E. Zaman, A review on underground hydrogen storage: insight into geological sites, influencing factors and future outlook, Energy Rep. 8 (2022) 461–499, https://doi.org/10.1016/j.egyr.2021.12.002.
[26] A. Lemieux, A. Shkarupin, K.R. Sharp, Geologic feasibility of underground hydrogen storage in Canada, Int. J. Hydrog. Energy 45 (56) (2020) 32243–32259, https://doi.org/10.1016/j.ijhydene.2020.08.244.
[27] R. Tarkowski, B. Uliasz-Misiak, P. Tarkowski, Storage of hydrogen, natural gas, and carbon dioxide – geological and legal conditions, Int. J. Hydrog. Energy 46 (38) (2021) 20010–20022, https://doi.org/10.1016/j.ijhydene.2021.03.131.

[28] E.I. Epelle, W. Obande, G.A. Udourioh, I.C. Afolabi, K.S. Desongu, U. Orivri, B. Gunes, J.A. Okolie, Perspectives and prospects of underground hydrogen storage and natural hydrogen, Sustain. Energy Fuels 6 (14) (2022) 3324–3343, https://doi.org/10.1039/d2se00618a.

[29] A.J. Phillips, E.G. Lauchnor, J. Eldring, R. Esposito, A.C. Mitchell, R. Gerlach, A. B. Cunningham, L.H. Spangler, Potential CO_2 leakage reduction through biofilm-induced calcium carbonate precipitation, Environ. Sci. Technol. 47 (1) (2012) 142–149, https://doi.org/10.1021/es301294q.

[30] C.M. Kirkland, A. Thane, R. Hiebert, R. Hyatt, J. Kirksey, A.B. Cunningham, R. Gerlach, L.H. Spangler, A.J. Phillips, Addressing wellbore integrity and thief zone permeability using microbially-induced calcium carbonate precipitation (MICP): a field demonstration, J. Pet. Sci. Eng. 190 (2020) 107060, https://doi.org/10.1016/j.petrol.2020.107060.

[31] O. Kolawole, I. Ispas, M. Kumar, J. Weber, B. Zhao, Time-lapse biogeomechanical modified properties of ultra-low permeability reservoirs, Rock Mech. Rock. Eng. 54 (2021) 2615–2641, https://doi.org/10.1007/s00603-021-02410-5.

[32] A. Almajed, H. Abbas, M.G. Arab, A.H. Alsabhan, W. Hamid, Y. Al-Salloum, Enzyme-Induced Carbonate Precipitation (EICP)-based methods for ecofriendly stabilization of different types of natural sands, J. Clean. Prod. 274 (2020) 122627, https://doi.org/10.1016/j.jclepro.2020.122627.

[33] K. Martin, H.K. Tirkolaei, E. Kavazanjian, Enhancing the strength of granular material with a modified enzyme-induced carbonate precipitation (EICP) treatment solution, Constr. Build. Mater. 271 (2021) 121529, https://doi.org/10.1016/j.conbuildmat.2020.121529.

[34] O. Kolawole, Mechanistic study of microbial altered properties in dolostones, Rock Mech. Rock. Eng. 56 (2) (2023) 1099–1111, https://doi.org/10.1007/s00603-022-03116-y.

[35] O. Kolawole, C. Millikan, M. Kumar, I. Ispas, B. Schwartz, J. Weber, L. Badurina, B. Šegvić, Data for: insights into the microbial-rock-CO_2 interactions in carbonates, in: Mendeley Data, V2, 2022, https://doi.org/10.17632/s6gvrztrrc.2.

[36] D. Landa-Marbán, S. Tveit, K. Kumar, S.E. Gasda, Practical approaches to study microbially induced calcite precipitation at the field scale, Int. J. Greenhouse Gas Control 106 (2021) 103256, https://doi.org/10.1016/j.ijggc.2021.103256.

[37] J.H. Yoon, K.C. Lee, N. Weiss, Y.H. Kho, K.H. Kang, Y.H. Park, *Sporosarcina aquimarina* sp. nov., a bacterium isolated from seawater in Korea, and transfer of *Bacillus globisporus* (Larkin and Stokes 1967), *Bacillus psychrophilus* (Nakamura 1984) and *Bacillus pasteurii* (Chester 1898) to the genus *Sporosarcina* as *Sporosarcina globispora* comb. nov., *Sporosarcina psychrophila* comb. nov. and *Sporosarcina pasteurii* comb. nov., and emended description of the genus *Sporosarcina*, Int. J. Syst. Evol. Microbiol. 51 (2001) 1079–1086, https://doi.org/10.1099/00207713-51-3-1079.

[38] W.F. Brace, J.B. Walsh, W.T. Frangos, Permeability of granite under high pressure, J. Geophys. Res. 73 (6) (1968) 2225–2236, https://doi.org/10.1029/JB073i006p02225.

[39] J. Bear, Dynamics of Fluids in Porous Media, Courier Corporation, 2013.

[40] A. Ebigbo, A. Phillips, R. Gerlach, R. Helmig, A.B. Cunningham, H. Class, L. H. Spangler, Darcy-scale modeling of microbially induced carbonate mineral precipitation in sand columns, Water Resour. Res. 48 (7) (2012), https://doi.org/10.1029/2011WR011714.

[41] J. Hommel, E. Lauchnor, A. Phillips, R. Gerlach, A.B. Cunningham, R. Helmig, A. Ebigbo, H. Class, A revised model for microbially induced calcite precipitation: improvements and new insights based on recent experiments, Water Resour. Res. 51 (5) (2015) 3695–3715, https://doi.org/10.1002/2014WR016503.

[42] E.G. Lauchnor, D. Topp, A. Parker, R. Gerlach, Whole cell kinetics of ureolysis by *Sporosarcina pasteurii*, J. Appl. Microbiol. 118 (6) (2015) 1321–1332, https://doi.org/10.1111/jam.12804.

[43] C.-Z. Qin, S.M. Hassanizadeh, A. Ebigbo, Pore-scale network modeling of microbially induced calcium carbonate precipitation: insight into scale dependence of biogeochemical reaction rates, Water Resour. Res. 52 (11) (2016) 8794–8810, https://doi.org/10.1002/2016WR019128.

[44] J. Hommel, A. Ebigbo, R. Gerlach, A.B. Cunningham, R. Helmig, H. Class, Finding a balance between accuracy and effort for modeling biomineralization, Energy Procedia 97 (2016) 379–386, https://doi.org/10.1016/j.egypro.2016.10.028.

[45] M. Thullner, J. Zeyer, W. Kinzelbach, Influence of microbial growth on hydraulic properties of pore networks, Transp. Porous Media 49 (2002) 99–122, https://doi.org/10.1023/A:1016030112089.

[46] K.-A. Lie, An Introduction to Reservoir Simulation Using MATLAB/GNU Octave: User Guide to the MATLAB Reservoir Simulation Toolbox (MRST), Cambridge University Press, 2019, https://doi.org/10.1017/9781108591416.

[47] K.-A. Lie, O. Møyner, Advanced Modelling With the MATLAB Reservoir Simulation Toolbox, Cambridge University Press, 2021.